

Barrier for cold-fusion production of superheavy elements

Takatoshi Ichikawa*

Advanced Science Research Center, Japan Atomic Energy Research Institute, Tokai-mura, Naka-gun, Ibaraki, 319-1195, Japan

Akira Iwamoto

Japan Atomic Energy Research Institute, Tokai-mura, Naka-gun, Ibaraki, 319-1195, Japan

Peter Möller and Arnold J. Sierk

Theoretical Division, Los Alamos National Laboratory, Los Alamos, New Mexico 87545, USA

(Received 5 November 2004; published 28 April 2005)

We estimate the fusion-barrier height $B_{\text{fu}}^{(\text{two-body})}$ for approaching ions in cold-fusion reactions in a model where the projectile deformation and quadrupole zero-point vibrational energy are taken into account. This barrier height is defined as the barrier energy at the target and projectile separation distance where an original oblate deformation of projectile and/or target caused by a repulsive Coulomb force turns into a large prolate deformation caused by the attractive nuclear force as the target and projectile come closer. The instability develops before touching because the attractive short-range nuclear force overcomes the repulsive Coulomb force *and* the shape-stabilizing effect of shell structure. The shell structure of the doubly magic ^{208}Pb target is sufficiently strong that its shape remains very close to spherical in all cases studied here. The fusion potential for approaching ions in the two-body channel is calculated in the macroscopic-microscopic model with the quadrupole vibrational zero-point energy obtained in the WKB approximation. We compare our results with data from 10 experimental cold-fusion reactions and with the Bass barriers. Differences and similarities between the Yukawa-plus-exponential model and the Bass model are discussed. We also calculate five-dimensional potential-energy surfaces for the single compound system and show that well-established fission and fusion valleys are both present. For heavy systems, $B_{\text{fu}}^{(\text{two-body})}$ becomes lower than the fission barrier just beyond the ground state of the compound system. In the vicinity of this transition, the optimum collision energy for formation of evaporation residues can be expected to depend in a delicate fashion on the interplay among $B_{\text{fu}}^{(\text{two-body})}$, the fusion valley, the fission barrier of the compound system, and the one- and two-neutron separation energies S_{1n} and S_{2n} . We discuss these issues in detail and calculate fission-barrier heights. Except for reactions in which the projectile is doubly magic or near doubly magic, the calculated quantities are consistent with the observed optimal energies for evaporation-residue formation.

DOI: 10.1103/PhysRevC.71.044608

PACS number(s): 25.70.Jj

I. INTRODUCTION

Heavy-ion fusion reactions have exclusively been chosen for synthesizing new elements beyond the actinides for several decades. Hot-fusion reactions led to the discovery of the elements with proton numbers $Z = 104$, 105, and 106, whereas the elements with $Z = 107$ –112 were first synthesized in cold-fusion reactions at GSI mbH, Darmstadt, Germany, during 1981–1996 [1]. Hot-fusion reactions were subsequently used at the Joint Institute for Nuclear Research in Dubna, Russia, in experiments designed to reach other isotopes of these elements and elements beyond [1–3]. Evidence for element $Z = 113$ was very recently observed at the RIKEN laboratory in Tokyo. [4]. The cross section for producing transactinide elements in these reactions decreases with increasing Z , is negligible outside a narrow energy window, and depends sensitively on the choice of target and projectile. Consequently, substantial effort has been dedicated to developing reaction theories that are sufficiently accurate to be useful in the design of experiments to produce new elements or new isotopes of known elements. However, the reaction processes leading to

such heavy systems are so complicated that a universally accepted model has yet to emerge. Here we focus on one part of such a theory, namely the fusion-barrier height $B_{\text{fu}}^{(\text{two-body})}$ for approaching ions in the two-body channel and its influence on the reaction. A further discussion of this concept in relation to the fusion barrier for the composite system $B_{\text{fu}}^{(\text{one-body})}$ will be given at the beginning of the next section. The fusion barrier is usually calculated by assuming spherical targets and projectiles. Here we develop a more realistic model of $B_{\text{fu}}^{(\text{two-body})}$ by allowing for target and projectile deformation, and we also calculate the contribution of the shell-energies to the self-energies of the deforming targets and projectiles. The changes in these self-energies give rise to significant effects on $B_{\text{fu}}^{(\text{two-body})}$ of the colliding system.

Both cold- and hot-fusion reactions have several features in common while differing in other important respects. For example, in hot-fusion reactions with actinide targets, the compound systems are formed at high excitation energy, about 40 MeV, whereas in cold-fusion reactions with targets close to ^{208}Pb , the compound systems in the $1n$ channel are typically formed at 10–15 MeV excitation energies. Here we limit our study to cold-fusion reactions, because with spherical targets, in contrast to the deformed targets in hot-fusion reactions,

*Electronic address: takichi@popsvr.tokai.jaeri.go.jp

they are the simpler of the two reaction mechanisms. Despite this greater simplicity, they are still not well understood. Furthermore, we emphasize entrance-channel effects. We feel the system is relatively free from dissipation, at least in the early stages on which we mainly concentrate here, but we do consider important microscopic effects on the potential energy, such as shell effects and quadrupole zero-point energies.

Evaporation-residue formation occurs only in a very narrow energy window. The optimal energy is believed to be correlated to the higher of (1) $B_{\text{fu}}^{(\text{two-body})}$ and (2) the sum of S_{1n} and the fission-barrier height [5]. Therefore, it is extremely important to accurately model $B_{\text{fu}}^{(\text{two-body})}$ and its dependence on the incoming projectile species. We previously developed a model and associated computer code [6] to calculate the macroscopic potential energy between two arbitrarily oriented, deformed heavy ions based on the Yukawa-plus-exponential model for the nuclear interaction energy [7] in addition to the standard Coulomb term. Cold-fusion barrier heights in the two-body channel obtained in this model for the standard deformation choice of spherical target and projectile are consistently higher than the optimal energy for $1n$ reactions. The barrier obtained is also higher than the phenomenological Bass barrier [8]. On the other hand, the calculated barrier heights are in good agreement with those obtained in calculations based on the double-folding potential of Hartree-Fock-Bogolyubov density distributions [9].

We expect that the differences between fusion-barrier heights obtained in simple calculations and experimental data are due to the absence in our model of some important dynamical effects. Obvious candidates for some of these effects are projectile and target deformations. Our calculations show that the target and projectile shell-correction deformation dependences give important contributions to the fusion barrier between the target and projectile. The magnitudes of the target and projectile shell corrections at infinity do not directly influence this barrier; however, they strongly influence the excitation energies of the resulting compound nuclei. Our calculations further show that the shell effects in the target Pb nucleus are so strong that although target deformations at some distances decrease the macroscopic total energy of the fusing system, the increase in shell-correction energies more than compensates for this decrease, so that the target nucleus remains nearly spherical. Because microscopic effects are extremely difficult to treat in a full-blown dynamical calculation, we do not carry out such calculations here. However, we do go considerably beyond the simple concept of a one-dimensional fusion barrier between spherical nuclei in a macroscopic model and determine a multidimensional “collision surface” for separated targets and projectiles. This object is a fusion potential-energy surface that is a function of target and projectile separation and of projectile deformation. Furthermore, we take microscopic effects into account when we calculate the collision surface by use of the macroscopic-microscopic method. We also study the potential energy for the composite one-body system that forms after touching by calculating macroscopic-microscopic potential-energy surfaces versus five different shape coordinates for more than 3×10^6 different shapes. We show that the potential outside

and inside touching match up in a way that may increase the probability for compound-nucleus formation. We find that for the composite system, there exists a valley that persists for a substantial part of the trajectory toward the compound system. The nuclear shapes corresponding to the initial part of this valley correspond closely to the shapes of the colliding ions just before touching. Therefore, the designation “fusion valley” is clearly appropriate. The valley is also stabilized by a ridge that is several MeV high. Thus, relative to a macroscopic picture, the probability that the trajectory will be deflected into the fission valley is decreased [10,11].

In the next section, we specify how we calculate the effect of projectile deformation and of quadrupole zero-point motion on the collision surface. In Sec. III, results of numerical calculations in this model are presented and compared with the Bass model. In Sec. IV, we discuss the fusion-fission potential-energy surface for the composite system. Sec. V is devoted to a comparison of results calculated in our model with experiments. A short summary is given in Sec. VI.

II. MODELS

In many proposed models of evaporation-residue cross sections in heavy-ion reactions, the initial part of the reaction is modeled in terms of a one-dimensional fusion barrier that exists between the approaching heavy ions. A few different models for this one-dimensional barrier are used. Usually only the maximum on this curve, the *fusion-barrier height*, enters into the models for the cross sections. It is often referred to as the Coulomb barrier (height). It is assumed that the maximum of the barrier occurs before or when the approaching ions touch.

Here we will introduce a multidimensional model for the fusion potential-energy *surface* of the approaching ions. We will also calculate multidimensional potential-energy surfaces for the composite, single system that is formed after the ions have come into contact. We will show in Sec. IV that for elongated shapes, these surfaces often exhibit two well-developed valleys of which one can be associated with fission and the other with the cold-fusion configurations that occur before the ions touch. Near ground-state shapes, these two valleys disappear; and when the collision process reaches the ground state, a compound system is formed.

Our aim here is to identify from our multidimensional calculations a value B_{fu} for the fusion-barrier height that is appropriate to use in reaction cross-section models that describe the fusion process in terms of a single barrier-height value. That is, it should be more appropriate to use than a value obtained from a simple one-dimensional model of the fusion potential.

To describe the above situation, we need to introduce some notation. From our model of the multidimensional potential, we will obtain a fusion-barrier height for approaching ions in the two-body channel $B_{\text{fu}}^{(\text{two-body})}$, which is already mentioned in the Introduction. When we consider cold-fusion collisions leading to heavier and heavier composite systems, we find that $B_{\text{fu}}^{(\text{two-body})}$ becomes lower and lower and may even become lower than the ground-state energy. For sufficiently heavy composite systems, B_{fu} is therefore no longer given

by $B_{\text{fu}}^{(\text{two-body})}$ but by some energy on the potential-energy surface of the composite one-body system between the touching configuration and the ground state, which we will call $B_{\text{fu}}^{(\text{one-body})}$. We have here consciously avoided the term ‘‘saddle-point energy’’ because both $B_{\text{fu}}^{(\text{one-body})}$ and $B_{\text{fu}}^{(\text{two-body})}$ may not correspond to a saddle point but to a point where a ridge that stabilizes a fusion valley disappears, or even to some other type of point on the multidimensional surface.

A. Potential energy in the two-body channel

We calculate the potential energy of colliding heavy ions in a model where deformations of the projectile and target are taken into account. At close range, the energetically favored target-projectile configuration is prolate-nuclei oriented in the tip-to-tip configuration having axial symmetry, which configuration has been referred to as the polar-parallel configuration [12]. We therefore limit the relative orientations studied to this orientation when we calculate the effect of induced target and projectile spheroidal deformations on $B_{\text{fu}}^{(\text{two-body})}$.

The potential energy of the system in the two-body channel is described as a function of the center-of-mass separation distance r and the target and projectile deformation parameters ϵ_T and ϵ_P , respectively. We use the spheroidal deformation parameter ϵ_2 of the Nilsson perturbed-spheroid parametrization [13]. The potential energy of the system is the sum of the macroscopic interaction energy E_{PT}^{int} and the macroscopic-microscopic self-energies of the projectile and target, E_P^{self} and E_T^{self} , respectively.

Therefore, the total potential energy of the system relative to the infinitely separated target and projectile is given by

$$E_{P+T}(r, \epsilon_{2T}, \epsilon_{2P}) = E_P^{\text{self}}(\epsilon_{2P}) - E_P^{\text{self}}(\epsilon_{2P}^{(0)}) + E_T^{\text{self}}(\epsilon_{2T}) - E_T^{\text{self}}(\epsilon_{2T}^{(0)}) + E_{PT}^{\text{int}}(r, \epsilon_{2T}, \epsilon_{2P}), \quad (1)$$

where $\epsilon_{2T}^{(0)}$ and $\epsilon_{2P}^{(0)}$ denote the deformation parameters of the target and the projectile in their ground states at infinite separation. Note that the self-energies at infinity include the ground-state quadrupole zero-point energies as discussed in [14].

The self-energies E^{self} of ^{208}Pb , ^{48}Ca , ^{64}Ni , and ^{74}Ge relative to the self-energies of corresponding spherical liquid drops are shown in Fig. 1 as functions of ϵ_2 . The macroscopic part is calculated in the macroscopic FRLDM model. The microscopic part is obtained as a sum of the shell- and pairing-correction energies by use of the Strutinsky method [15,16]. Full details of the model are given in Ref. [17].

The interaction energy E_{PT}^{int} consists of the nuclear interaction energy, calculated in the Yukawa-plus-exponential macroscopic model [7,14,17], and the Coulomb interaction energy. We assume that the interaction shell-correction energy can be neglected for the separated target and projectile. The interaction surface and Coulomb energies are given by

$$E_S^{\text{int}} = -\frac{c_s}{4\pi^2 r_0^2 a^3} \int_{V_T} \int_{V_P} \left(\frac{\sigma}{a} - 2 \right) \frac{e^{-\sigma/a}}{\sigma} d^3 r d^3 r', \quad (2)$$

$$E_C^{\text{int}} = \int_{V_T} \int_{V_P} \frac{1}{\sigma} \rho_T(\mathbf{r}) \rho_P(\mathbf{r}') d^3 r d^3 r', \quad (3)$$

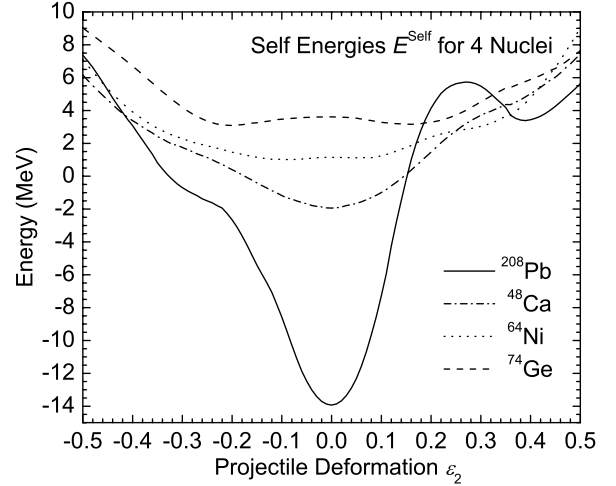


FIG. 1. Self-energies of ^{208}Pb , ^{48}Ca , ^{64}Ni , and ^{74}Ge calculated in the macroscopic-microscopic model, as functions of the deformation ϵ_2 . Energies are plotted relative to the self-energies of a spherical liquid drop.

respectively, where $\sigma = |\mathbf{r} - \mathbf{r}'|$ and $\rho_T(\mathbf{r})$ and $\rho_P(\mathbf{r})$ denote the charge densities of the target and projectile at point \mathbf{r} , respectively. V_T and V_P are the regions of the volume integral for the target and projectile, respectively. From Refs. [14,17], we adopt

$$\rho_T = \frac{3}{4\pi} \frac{Z_T e}{(r_T A_T^{1/3})^3}, \quad \rho_P = \frac{3}{4\pi} \frac{Z_P e}{(r_P A_P^{1/3})^3}, \quad (4)$$

$$c_s = [c_s^{(T)} c_s^{(P)}]^{1/2}, \quad (5)$$

$$c_s^{(T)} = a_s (1 - \kappa_s I_T^2), \quad c_s^{(P)} = a_s (1 - \kappa_s I_P^2), \quad (6)$$

$$I_T = \frac{N_T - Z_T}{N_T + Z_T}, \quad I_P = \frac{N_P - Z_P}{N_P + Z_P}, \quad (7)$$

where $a_s = 21.33$ MeV, $\kappa_s = 2.3785$, $a = 0.68$ fm, and $r_T = r_P = r_0 = 1.16$ fm are chosen as in the readjusted FRLDM [18] and Z and N denote the proton and neutron numbers, respectively. We assume that the charge densities of the target and projectile ρ_T and ρ_P are constant. The calculation of the interaction-energy term is extensively discussed in Ref. [6].

In the case of cold-fusion reactions with ^{208}Pb targets, where the bombarding energy of the projectile is in the vicinity of $B_{\text{fu}}^{(\text{two-body})}$, we have, as discussed in the Introduction, calculated that the target remains spherical because of the stabilizing influence of the shell structure (Fig. 1). For example, we have calculated the potential energy for the system $^{50}\text{Ti} + ^{208}\text{Pb}$ as given by Eq. (1) as a function of the deformations of the target and projectile at each center-of-mass separation r . By finding a local minimum in the potential-energy surface, we determined the energetically favorable deformations of the target and projectile at each center-of-mass separation. The deformations obtained are shown in Fig. 2. It is clear that we can safely assume the target remains spherical. At large r , the projectile shape is oblate because of Coulomb repulsion.

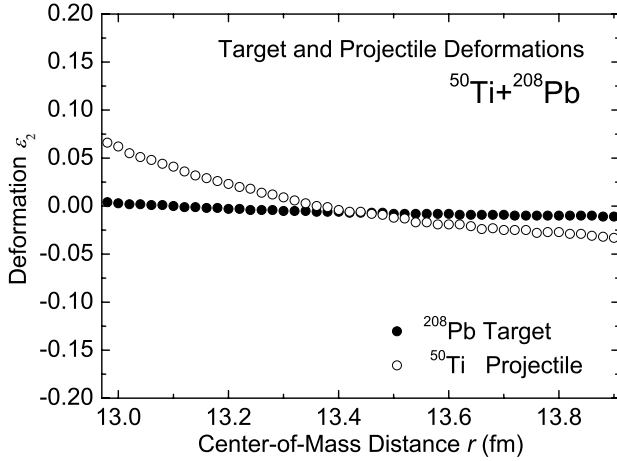


FIG. 2. Target and projectile deformations as functions of the center-of-mass distance r . At each separation r , the target and projectile deformations correspond to the local minimum in the potential-energy surface.

When the projectile comes closer to the target, the projectile tends to become prolate because of the onset of the short-range nuclear attraction. With the assumption of a spherical target, the potential energy in the two-body channel in cold-fusion reactions with ^{208}Pb targets simplifies to

$$E_{P+T}(r, \epsilon_{2P}) = E_P^{\text{self}}(\epsilon_{2P}) - E_P^{\text{self}}(\epsilon_{2P}^{(0)}) + E_{PT}^{\text{int}}(r, \epsilon_{2P}). \quad (8)$$

We start the calculation of the potential energy from the center-of-mass separation $r = 15$ fm, far outside the peak in the fusion barrier in the two-body channel. The potential energy is then calculated for a succession of separations $r = 14.98, 14.96,$ and 14.94 fm until we reach a separation corresponding to touching spherical target and projectile. At each separation, the energy is calculated for a large number of densely spaced projectile deformations chosen so that the total potential-energy-surface minimum of the system is always included.

Figure 3 shows the potential energy for the $^{64}\text{Ni} + ^{208}\text{Pb}$ system as a function of the projectile deformation for a succession of different center-of-mass separations r . At around $r = 14.0$ fm, a prolate, second minimum develops, separated from the oblate minimum by a low saddle. Eventually the system loses stability with respect to projectile deformation, and in our model this is where a composite system is formed. We now discuss how we define and determine the point of instability and the $B_{\text{fu}}^{(\text{two-body})}$ associated with this instability.

Figure 4 shows in more detail the potential-energy curve for $^{64}\text{Ni} + ^{208}\text{Pb}$ at a center-of-mass separation $r = 13.54$ fm. A number of target and projectile configurations at this center-of-mass separation are also shown. The energy of the local, slightly oblate minimum is 239.82 MeV. For this configuration, the vibrational zero-point energy (0.32 MeV) has become just about equal to the highest of the two relative saddle-point heights (in this case, the rightmost saddle point). Therefore, stability with respect to projectile deformation is lost, and

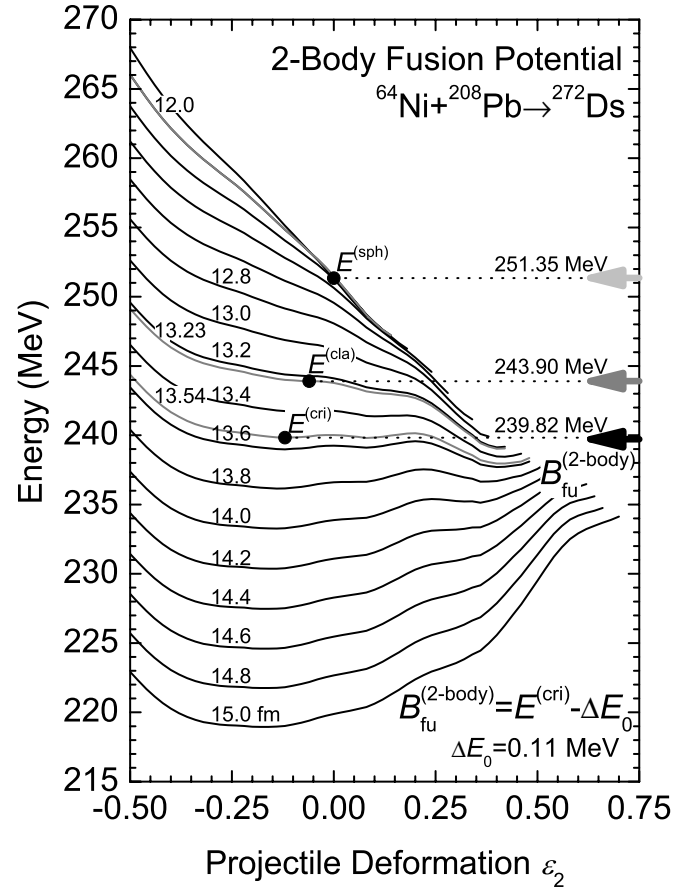


FIG. 3. Potential-energy curves as functions of the projectile deformation ϵ_2 at various separations r from a spherical ^{208}Pb target. The solid lines show the potential energy at each center-of-mass separation. The system becomes unstable with respect to projectile deformation at $r = 13.54$ fm where the quadrupole zero-point energy exceeds the energy of the highest of the saddle points separating the minimum from the low-energy region at large projectile deformation that corresponds to the touching configuration. $E^{(\text{cri})}$ is the energy of the local minimum at the critical distance where stability is lost. The black arrow points to the fusion-barrier height in the two-body channel $B_{\text{fu}}^{(\text{two-body})}$, which is defined as $B_{\text{fu}}^{(\text{two-body})} = E^{(\text{cri})} - \Delta E_0$, where ΔE_0 is the difference between the zero-point energies at infinite separation and at the critical distance. $E^{(\text{cla})}$ and $E^{(\text{sph})}$ denote the energies where the classical instability (see Sec. II B for a definition) occurs and the spherical barrier energy, respectively. The medium-gray and the light-gray arrows show $E^{(\text{cla})}$ and $E^{(\text{sph})}$, respectively.

a composite system can form. The energy of the potential-energy minimum at this critical separation $r^{(\text{cri})}$ where the projectile has just lost stability with respect to deformation is designated $E^{(\text{cri})}$. Other situations may also occur. At the starting separation 15.00 fm, we identify the lowest minimum which defines the initial projectile deformation. If a second lower minimum develops for smaller separations, we check at each separation if the saddle separating the two minima is higher than the zero-point energy of the system in the original minimum. If it is not, then the lower minimum will

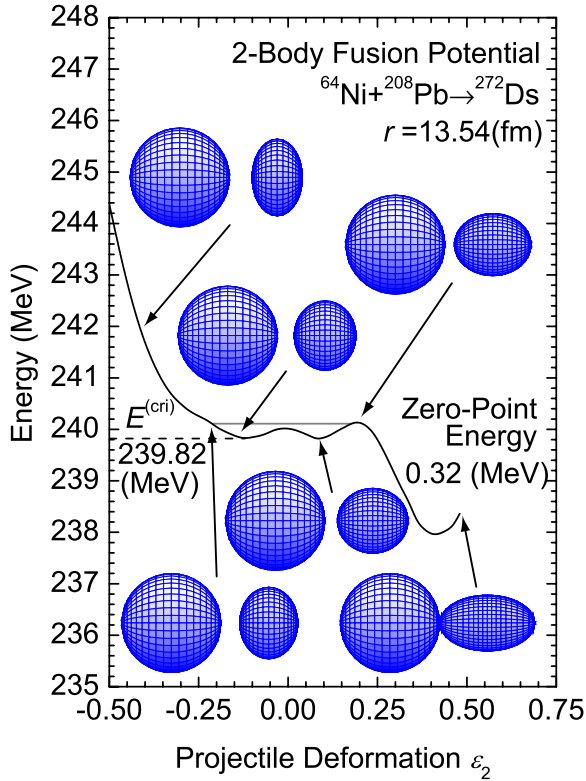


FIG. 4. (Color online) Potential-energy curve as a function of the projectile deformation ϵ_2 at the critical distance $r = 13.54$ fm. System shape configurations at representative deformations are also plotted. For this particular center-of-mass separation, the projectile and target are in contact at $\epsilon_2 = 0.5$. The thin, solid horizontal line denotes the zero-point energy calculated in the WKB approximation. The local energy minimum at the critical distance is $E^{(cri)}$.

correspond to a new system configuration. We then check, for this separation, if the new zero-point energy is higher than the maximum between this local minimum and the new minimum near touching. In that case, the system forms a composite system, otherwise it does not. Because the curves plotted do not contain the zero-point energy contributions to the self-energies, $B_{fu}^{(two-body)}$ is not exactly $E^{(cri)}$. The definition of $B_{fu}^{(two-body)}$ and the calculation of the zero-point energy are discussed in the next subsection.

B. Definition of fusion-barrier height in the two-body channel

Because the potential energy shown in Fig. 3 does not contain the zero-point energies in the self-energy terms, the fusion-barrier height $B_{fu}^{(two-body)}$ is given by

$$B_{fu}^{(two-body)} = E^{(cri)} - \Delta E_0, \quad (9)$$

where ΔE_0 given by

$$\Delta E_0 = E_0^{(\infty)} - E_0^{(cri)} \quad (10)$$

is the difference between the projectile zero-point energies at infinity and at the critical distance.

We calculate the zero-point energy in the WKB approximation, and determine whether the minimum is sufficiently deep that a bound state exists. In the WKB approximation, we obtain the zero-point energy E_0 by solving

$$2 \int_b^a \sqrt{2B(\epsilon_2)[E_0 - V(\epsilon_2)]} d\epsilon = \pi\hbar, \quad (11)$$

where a and b are the upper and lower limits of the positive range of the integrand, V denotes the potential energy, and B is the inertial mass with respect to ϵ_2 deformations.

The quantity B is obtained from $B = B^{ir}/K^2$, where B^{ir} is the hydrodynamical mass in the irrotational-flow approximation and $K = 0.33$ is a factor determined to optimally reproduce spontaneous-fission half-lives for actinide nuclei [14,19]. In the irrotational-flow approximation, the mass B^{ir} is given by

$$B^{ir}(\epsilon_2) = B^{ir}(0) \left(1 - \frac{1}{3}\epsilon_2^2 - \frac{2}{27}\epsilon_2^3 \right)^{-\frac{4}{3}} \frac{1 + \frac{2}{9}\epsilon_2^2}{(1 - \frac{2}{3}\epsilon_2)^2}, \quad (12)$$

where $B^{ir}(0)$ denotes the irrotational mass of the spherical nucleus, which is chosen as $B^{ir}(0) = 0.004632A^{5/3}\hbar^2 \text{ MeV}^{-1}$ from Ref. [20].

In the $^{64}\text{Ni} + ^{208}\text{Pb}$ system, $r = 13.54$ fm corresponds to the critical distance where the zero-point energy level of the projectile equals the saddle-point energy. At this distance the energy $E^{(cri)} = 239.82$ MeV and $\Delta E_0 = 0.11$ MeV. Therefore, the fusion barrier in two-body channel $B_{fu}^{(two-body)}$ is 239.71 MeV.

To show the effect of the zero-point vibrations and the deformation of the projectile, we also estimate the spherical barrier $B_{fu}^{(sph)}$ without any target and projectile deformation. This spherical barrier $B_{fu}^{(sph)}$, indicated by a light gray arrow in Fig. 3, is 251.35 MeV. Thus, we find that $B_{fu}^{(two-body)}$ is lower than $B_{fu}^{(sph)}$ by 11.64 MeV. To specifically establish the influence of considering the projectile spheroidal vibrational zero-point energies, we also calculate where the instability with respect to projectile deformation occurs if we ignore the zero-point energy (or equivalently assume it is zero). This situation we call ‘‘classical instability,’’ and it occurs at $r = 13.20$ fm at an energy $E^{(cla)} = 243.90$ MeV, shown by the darker gray arrow in Fig. 3.

III. FUSION POTENTIAL IN THE TWO-BODY CHANNEL

A. Calculated fusion-barrier height in the two-body channel

We calculate $B_{fu}^{(two-body)}$ for cold-fusion reactions with ^{48}Ca , ^{50}Ti , ^{54}Cr , ^{58}Fe , ^{62}Ni , ^{64}Ni , ^{70}Zn , ^{74}Ge , and ^{76}Ge projectiles incident on ^{208}Pb targets. We also determine $B_{fu}^{(two-body)}$ in cold-fusion reactions with ^{58}Fe , ^{64}Ni , and ^{76}Ge projectiles incident on ^{209}Bi targets. We assume that ^{209}Bi remains spherical in shape because of its similarity to ^{208}Pb , something we have also checked in actual three-dimensional calculations. In these calculations, the fusion potential is determined for successively

TABLE I. Calculated fusion-barrier heights $B_{\text{fu}}^{(\text{two-body})}$ for various systems. For comparison, we also tabulate the Bass barrier $B_{\text{fu}}^{(\text{Bass})}$ calculated with parameters Bass80 [8] and the spherical barrier $B_{\text{fu}}^{(\text{sph})}$. $E^{(\text{cla})}$ is the energy where the classical instability occurs. $E^{(\text{cri})}$ is the energy at the critical distance of approach, see text. ΔE_0 is the difference between the projectile zero-point energies at infinite separation and at the critical distance. $B_{\text{fu}}^{(\text{two-body})} - E_{\text{GS}}$ gives the fusion-barrier height measured from the ground state of the compound nucleus. E_{GS} is obtained from [17].

System	$B_{\text{fu}}^{(\text{Bass})}$ (MeV)	$B_{\text{fu}}^{(\text{sph})}$ (MeV)	$E^{(\text{cla})}$ (MeV)	$E^{(\text{cri})}$ (MeV)	ΔE_0 (MeV)	$B_{\text{fu}}^{(\text{two-body})}$ (MeV)	$B_{\text{fu}}^{(\text{two-body})} - E_{\text{GS}}$ (MeV)
$^{48}\text{Ca} + ^{208}\text{Pb} \rightarrow ^{256}\text{No}$	176.12	182.65	181.10	180.02	0.34	179.68	26.08
$^{50}\text{Ti} + ^{208}\text{Pb} \rightarrow ^{258}\text{Rf}$	193.90	201.04	197.21	195.28	0.26	195.03	24.09
$^{54}\text{Cr} + ^{208}\text{Pb} \rightarrow ^{262}\text{Sg}$	210.42	218.31	211.00	209.26	-0.25	209.51	21.08
$^{58}\text{Fe} + ^{208}\text{Pb} \rightarrow ^{266}\text{Hs}$	226.82	235.46	227.65	224.28	0.40	223.89	18.43
$^{62}\text{Ni} + ^{208}\text{Pb} \rightarrow ^{270}\text{Ds}$	243.11	252.52	245.33	239.59	-0.18	239.77	16.61
$^{64}\text{Ni} + ^{208}\text{Pb} \rightarrow ^{272}\text{Ds}$	241.88	251.35	243.90	239.82	0.11	239.71	15.08
$^{70}\text{Zn} + ^{208}\text{Pb} \rightarrow ^{278}\text{112}$	256.83	267.14	257.91	253.90	0.22	253.68	8.71
$^{74}\text{Ge} + ^{208}\text{Pb} \rightarrow ^{282}\text{114}$	272.88	283.96	281.26	271.47	-0.34	271.81	10.68
$^{76}\text{Ge} + ^{208}\text{Pb} \rightarrow ^{284}\text{114}$	271.68	282.85	276.88	270.62	0.24	270.38	7.31
$^{58}\text{Fe} + ^{209}\text{Bi} \rightarrow ^{267}\text{Mt}$	229.57	238.28	230.27	226.86	0.38	226.48	17.35
$^{64}\text{Ni} + ^{209}\text{Bi} \rightarrow ^{273}\text{111}$	244.81	254.35	246.72	242.59	0.10	242.49	13.85
$^{70}\text{Zn} + ^{209}\text{Bi} \rightarrow ^{279}\text{113}$	259.95	270.34	260.89	256.97	0.24	256.74	7.89

decreasing values of the center-of-mass separation r for $r = 15.00, 14.98, \dots, r^{(\text{cri})}$ where r is in units of fm. The critical distance $r^{(\text{cri})}$ and the fusion potential at $r^{(\text{cri})}$ are determined as discussed in the previous section.

Table I shows $B_{\text{fu}}^{(\text{two-body})}$ for various systems. To show the effect of deformations and vibrations, the spherical barrier height $B_{\text{fu}}^{(\text{sph})}$ is also tabulated. Because the Bass model is commonly used to model heavy-ion fusion barriers, we include the Bass barriers heights $B_{\text{fu}}^{(\text{Bass})}$ in Table I so that we can compare them to our results. The differences between our $B_{\text{fu}}^{(\text{two-body})}$ and Bass barrier heights are about ± 3.5 MeV. The definitions of the tabulated quantities are further discussed in the table caption and in the previous section.

Figure 5 shows the difference between $B_{\text{fu}}^{(\text{two-body})}$ and the spherical barrier height $B_{\text{fu}}^{(\text{sph})}$ for each of the studied systems. We see that $B_{\text{fu}}^{(\text{two-body})}$ is always lower than the spherical barrier height. To show the effect of the zero-point vibrations, the differences between the spherical barrier height and the critical energy at the classical instability are also presented. Except for reactions with the three very lightest projectiles near Ca, $B_{\text{fu}}^{(\text{two-body})}$ are consistently lower than $B_{\text{fu}}^{(\text{sph})}$ by about 13 MeV. For the reactions with ^{48}Ca and ^{50}Ti , the effect of vibrations and deformations is relatively small compared to the other systems, possibly because of the doubly magic or near doubly magic nature of the projectiles. However, despite the large stiffness of ^{48}Ca , $B_{\text{fu}}^{(\text{two-body})}$ is lower than $B_{\text{fu}}^{(\text{sph})}$ by about 3 MeV. This result shows the importance of deformation effects in the two-body channel, even when the projectile is fairly stiff as a result of shell effects.

For ^{74}Ge and ^{76}Ge , the difference between $B_{\text{fu}}^{(\text{two-body})}$ and the energy at the classical instability is much larger than for other systems. Although the energy at the classical instability for ^{74}Ge is lower than the spherical barrier height by only 2 MeV, $B_{\text{fu}}^{(\text{two-body})}$ for ^{74}Ge is lower than the spherical barrier by

about 12 MeV. This result comes from the self-energy of ^{74}Ge , which is shown as a function of deformation in Fig. 1. Two minima are separated by a local saddle centered around $\epsilon_2 = 0$. The oblate minimum is somewhat deeper and stiffer than the prolate minimum. When ^{74}Ge approaches the target, ^{74}Ge becomes oblate in shape because of the increasing Coulomb repulsion. The oblate shape minimum in the self-energy enhances the stability against prolate deformations. Thus, the critical energy at the classical instability becomes relatively high. However, the vanishing of the zero-point energy mainly

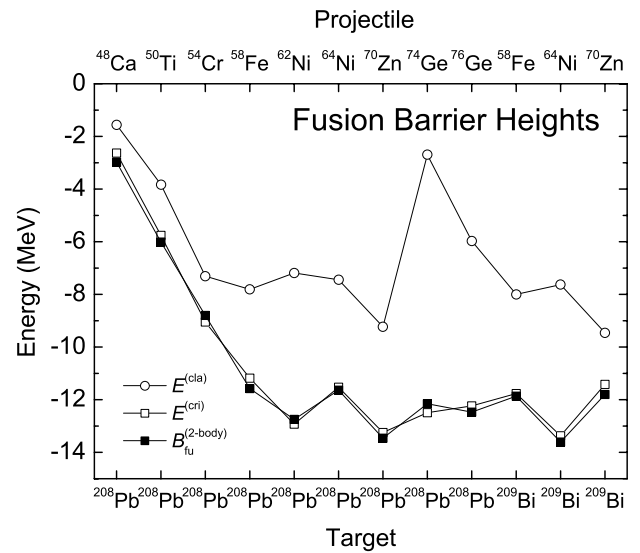


FIG. 5. Energies of various fusion-barrier quantities relative to the spherical barriers for several different cold-fusion reactions. The solid squares denote $B_{\text{fu}}^{(\text{two-body})}$ relative to the spherical barrier height $B_{\text{fu}}^{(\text{sph})}$. The energies $E^{(\text{cla})}$ and $E^{(\text{cri})}$ relative to $B_{\text{fu}}^{(\text{sph})}$ are denoted by open circles and open squares, respectively.

depends on the height of the saddle point in the fusion potential in the two-body channel. The change of the height of the saddle point is related to the curvature of the self-energy at large prolate deformations. The curvature around $\epsilon_2 = 0.3$ for ^{74}Ge is very similar to other systems. Therefore, $B_{\text{fu}}^{(\text{two-body})}$ for ^{74}Ge roughly decreases to the same extent as in other systems. These results indicate that both deformations and zero-point vibrations are very important in the two-body channel.

B. Comparison with Bass model results

Because the Bass model [8] has been extensively used to estimate fusion-barrier heights in heavy-ion reactions, with results similar to those obtained in our current model, cf. Fig. 9, we compare the main features of the respective models. We calculate the Bass barriers with the parameters from Ref. [8]. For ^{48}Ca and ^{50}Ti , the Bass model overestimates the peak energy of the $1n$ reaction, just as our model does. For projectiles heavier than ^{54}Cr , $B_{\text{fu}}^{(\text{two-body})}$ and Bass barrier height become closer to the peak energy of the $1n$ reactions. There are no large differences between $B_{\text{fu}}^{(\text{two-body})}$ and the Bass barrier heights over the range of reactions studied here. To learn why, we compare some major aspects of the Bass model and our calculation. The nuclear potential part V_N in the Bass model is given by

$$V_N^{(\text{Bass})}(s) = -\frac{R_1 R_2}{R_1 + R_2} \left[C_1 \exp\left(\frac{s}{d_1}\right) + C_2 \exp\left(\frac{s}{d_2}\right) \right]^{-1}, \quad (13)$$

where s denotes the distance between the surfaces of the projectile and the target. In Ref. [8] we find that $C_1 = 0.0061 \text{ MeV}^{-1} \text{ fm}$, $d_1 = 0.65 \text{ fm}$, $C_2 = 0.33 \text{ MeV}^{-1} \text{ fm}$, $d_2 = 3.3 \text{ fm}$, and the nuclear radius $R_i = 1.16A^{1/3} - 1.39A^{-1/3} \text{ fm}$, where A is the nucleon number. When the projectile and target are at large separation, in the Bass model, $V_N^{(\text{Bass})}$ is proportional to $\exp(-s/d_1)$. On the other hand, in the case of separated spherical nuclei, Eq. (2) can be approximated [7] by

$$V_N^{(\text{YPE})}(s) \sim -\frac{ac_s R_1 R_2}{r_0^2 (R_1 + R_2)} \left(2 + \frac{s}{a} \right) \exp\left(-\frac{s}{a}\right). \quad (14)$$

In Eq. (14), the middle factor $(2 + s/a)$ is due to the saturating condition of the nuclear force. At large center-of-mass separation, $V_N^{(\text{YPE})}$ is determined mainly by the factor $\exp(-s/a)$. Thus, it seems that d_1 in the Bass model corresponds to the effective range a of the folding function in the Yukawa-plus-exponential (YPE) model. The value 0.65 for d_1 is also consistent with the commonly used parameter of the folding function. However, when the projectile and target approach each other, the term $C_2 \exp(s/d_2)$ in the Bass model becomes dominant. This corresponds to a large increase in the effective range of the folding function in the YPE model. Although the effective range in the YPE model also increases by the saturating property, this effect is much smaller than the effective range in the Bass model. The large change in the effective range in the Bass model cannot be explained as due only to the saturating condition of the nuclear force. We suggest that in the Bass model, the effects of the zero-point vibration and the deformation are effectively simulated

through the term $C_2 \exp(s/d_2)$, but at a considerably more phenomenological level than in our treatment of these effects. In our treatment, no additional parameters or new parameter values are introduced relative to our standard FRLDM nuclear mass and fission-barrier model [17,18]; it is just applied in a straightforward way to fusion-barrier calculations.

IV. COMPOSITE-SYSTEM FUSION-FISSION POTENTIAL

The model for the two-body-channel potential presented in the previous section shows that the shape configuration when the touching configuration is reached consists of a projectile with a large prolate deformation and an almost spherical target. Inside touching, we can study the potential energy surface in our macroscopic-microscopic model for all shapes accessible to our three-quadratic-surface parametrization. This means that we will obtain a potential-energy surface that is appropriate to both fission and fusion. The highest fission saddle point for these heavy composite systems corresponds to shapes that are just a little more deformed than the ground state, and this saddle point is calculated in the ϵ parametrization, as mentioned above. The height of this saddle point influences the competition between fission and neutron evaporation once the compound system is formed. Also, when $B_{\text{fu}}^{(\text{two-body})}$ is lower than this saddle height, this saddle point is usually the maximum of the fusion barrier, which was defined as B_{fu} in Sec. II. For a few systems in the transition region between these two limiting situations, one can expect that B_{fu} instead corresponds to some point on the ridge between the fusion and fission valleys. In these cases, however, it may be impossible to provide a realistic model of the evaporation-residue cross section without detailed dynamical modeling of microscopic effects along the trajectory inside touching. For shapes more deformed than the inner saddle point, our calculated five-dimensional potential-energy surfaces present a structure that includes both a fission valley and a fusion valley. We find that the shape configuration of the single system in the fusion valley bears a very strong resemblance to the target and projectile shapes just at touching.

The five-dimensional macroscopic-microscopic potential-energy surfaces for composite one-body systems reached in cold-fusion heavy-ion reactions are calculated and analyzed using the same techniques as introduced previously in studies of actinide fission. In particular, we calculate the potential energy as a function of five nuclear-shape coordinates: 15 points each in the neck diameter and left and right fragment deformations, 35 points in the mass asymmetry, and 33 points in the nuclear elongation. This leads to a space of 3 898 125 grid points. However, as explained elsewhere [21] some grid-point coordinate values do not correspond to physically realizable shapes; therefore, the actual number of grid points considered is 3 594 915. Compared to our previous fission studies, we have increased the number of mass-asymmetry values from 20 to 35. The extension to such large mass asymmetries means that the expected cold-fusion channel near mass division 208/70 for the compound system $^{278}112$ is included in our calculated potential-energy surface. The distance between the grid points in the mass-asymmetry coordinate is 2.78 mass units for this compound system. More

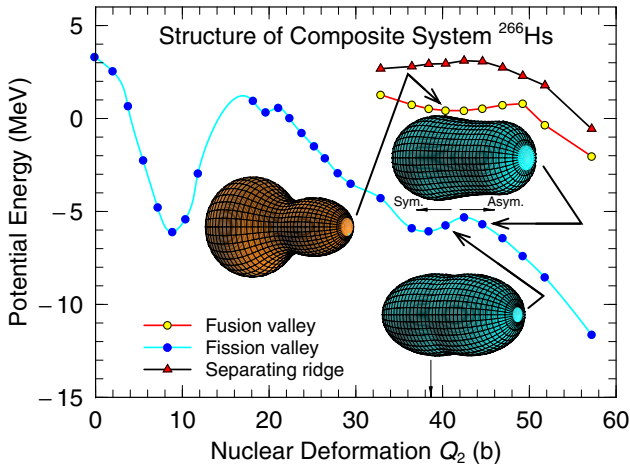


FIG. 6. (Color online) Structures in the calculated five-dimensional potential-energy surface of ^{266}Hs . The lower curve corresponds to the fission barrier. For large values of Q_2 , an additional well-defined valley occurs, which is stabilized with respect to the fission valley by the ridge shown in the top curve. Two shapes in the fission valley and one shape in the additional valley are shown. The shapes in the fission valley indicate that a transition to asymmetric shapes takes place around $Q_2 = 43$. The shape in the other valley corresponds to $M_H/M_L = 197/70$. The position of the vertical thin arrow on the horizontal axis indicates the value of Q_2 for the touching spherical target and projectile.

generally, for a compound nucleus with mass A the grid-point distance in the mass-asymmetry coordinate is $A/100$.

In Figs. 6–8, we show the result of a water-immersion analysis of the calculated five-dimensional deformation spaces for composite one-body systems corresponding to ^{266}Hs , ^{272}Ds , and $^{284}114$. The results are plotted versus the charge quadrupole moment Q_2 of a ^{240}Pu nucleus of the same shape as the nucleus being considered, so that the nuclear size and charge effects are eliminated. For each system, we have identified a fission barrier, which only exists because of

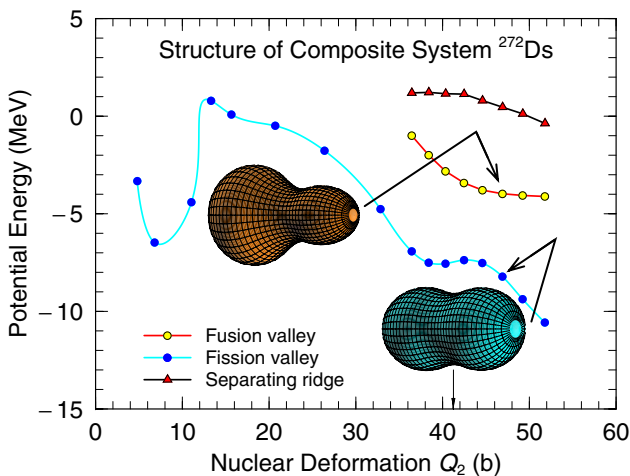


FIG. 7. (Color online) Same as Fig. 6, but for ^{272}Ds . The shape in the fission valley is symmetric, and the shape in the other valley corresponds to $M_H/M_L = 201/71$.

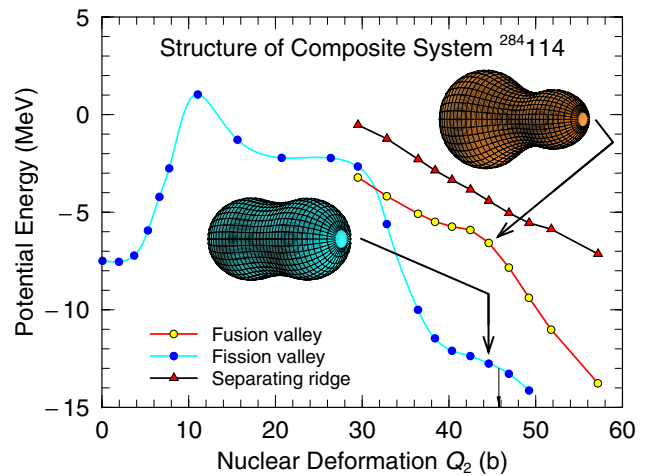


FIG. 8. (Color online) Same as Fig. 6, but for $^{284}114$. The shape in the fission valley is symmetric, and the shape in the other valley corresponds to $M_H/M_L = 213/71$.

large, negative microscopic corrections at the ground state, giving rise to a fission barrier that is high enough that these nuclei survive for a sufficiently long time to permit experimental study. For larger deformations, all three figures also show a second valley that our water-immersion analysis has identified, as well as the ridge which stabilizes this valley with respect to the fission valley. The asymmetry of shapes in the secondary valley as well as their deformations strongly overlap with the target and projectile mass ratios and deformations in the two-body channel. A little loosely we could say that the colliding projectile and target after touching will slip into this valley as a hand slips into a glove. Of course, the energy of this valley is often 10 MeV or more lower than the energy of the fusion collision potential-energy surface saddle discussed before. However, this is mainly because the composite one-body shapes we study have developed a substantial neck, which significantly lowers the energy. This appearance of the potential-energy surface is very different from that obtained in a macroscopic multidimensional picture in which these systems just after touching find themselves on a surface that slopes steeply sideways relative to the incident direction. These systems colliding “at the Coulomb barrier” would immediately be deflected to the fission valley and re-separation [10,22,23]. Thus, we have identified an additional effect that favors cold fusion: microscopic effects in the composite one-body system potential-energy surface create a shell-stabilized valley that is basically a continuation of the two-body-channel configuration that has developed at the critical distance. It remains to deduce the effect of how relative differences between systems in the calculated barriers and ridges, and associated dynamical effects such as damping, affect the evaporation-residue cross sections.

V. COMPARISON WITH EXPERIMENTS

In Fig. 9, we compare $B_{fu}^{(two-body)}$, denoted by black arrows, to experimental evaporation-residue cross sections. The spherical barrier heights and the energies at the classical

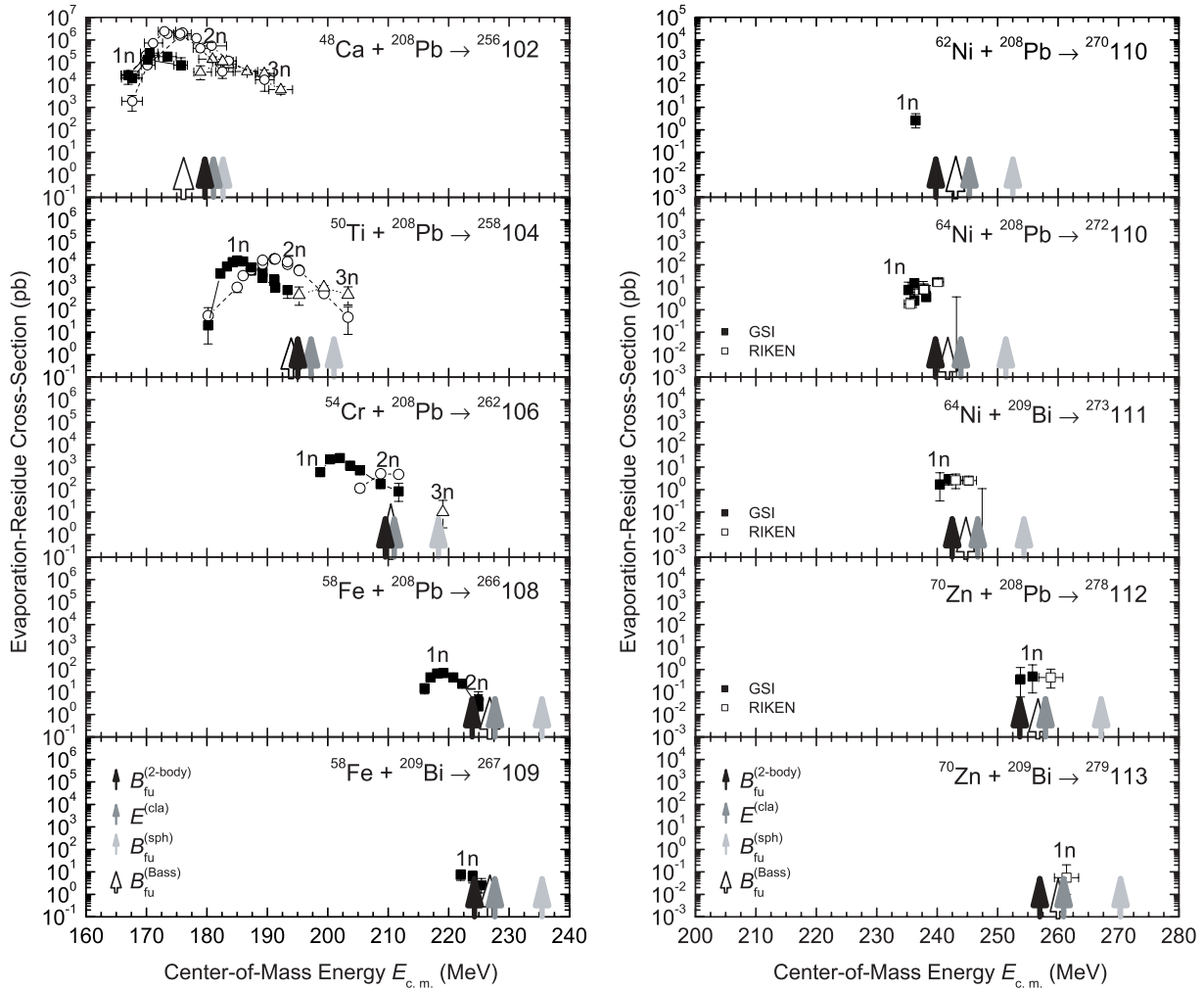


FIG. 9. (Color online) Calculated barrier heights compared to experimental data. The experimental data for $^{48}\text{Ca} + ^{208}\text{Pb}$ are taken from Refs. [24–26]. The experimental data for ^{50}Ti , ^{54}Cr , ^{58}Fe , ^{62}Ni , ^{64}Ni , $^{70}\text{Zn} + ^{208}\text{Pb}$ and ^{58}Fe , $^{64}\text{Ni} + ^{209}\text{Bi}$ are from Refs. [1,27,28]. The solid squares denote the measured evaporation-residue cross section for the $1n$ -reaction branch. The fusion-barrier heights $B_{\text{fu}}^{(2\text{-body})}$ are shown as black arrows. $B_{\text{fu}}^{(\text{sph})}$ and $E^{(\text{cri})}$ are shown as light-gray and darker-gray arrows, respectively. As a comparison, the Bass barrier heights $B_{\text{fu}}^{(\text{Bass})}$ are shown as open arrows.

instability are also shown as medium-gray and light-gray arrows, respectively. The solid points denote the excitation function for the evaporation-residue formation for 10 reactions for which experimental data are available from GSI [1,27,28], Dubna [24–26], and RIKEN [4,30,31].

From Fig. 9, it is seen that the calculated fusion-barrier heights in the two-body channel $B_{\text{fu}}^{(2\text{-body})}$ are considerably higher than the peaks of the $1n$ channel for the reactions with ^{48}Ca , ^{50}Ti , and ^{54}Cr . With increasing projectile mass number, the calculated $B_{\text{fu}}^{(2\text{-body})}$ becomes close to the peak energy of the $1n$ reactions. Although the data are less complete for these heavy systems, our calculated barrier heights $B_{\text{fu}}^{(2\text{-body})}$ appear to have energies similar to those at the peak of the $1n$ reaction for ^{58}Fe , ^{62}Ni , ^{64}Ni , and ^{70}Zn projectiles incident on ^{208}Pb targets, to within a few MeV or so.

When we discuss the systematics of the evaporation-residue cross section, we need to recall that it depends not only on

$B_{\text{fu}}^{(2\text{-body})}$ but also on $B_{\text{fu}}^{(\text{one-body})}$ and dynamics after touching and on the survival probability of the compound system, if it forms. The compound-nucleus formation probability will be affected by the fission saddle just beyond the ground-state minimum, particularly if it is higher than $B_{\text{fu}}^{(2\text{-body})}$, as is the case for the heavier of the systems we study here. The height and length or persistence of the ridge that inside touching separates the two-body-channel fusionlike valley from the fission valley will also affect the compound-nucleus formation cross section. If formed, the compound-nucleus survival probability is determined by the competition between the fission and neutron-evaporation probabilities. In addition, whether $1n$ or $2n$ channels become favorable roughly correlates with the sum of the fission-barrier height and the $1n$ -neutron separation energy $B_{\text{fi}} + S_{1n}$ and the $2n$ -separation energy S_{2n} [5]. For the systems presented in Table I, we obtain evidence that most $B_{\text{fi}} + S_{1n}$ are lower than S_{2n} . Thus, we expect that the $1n$

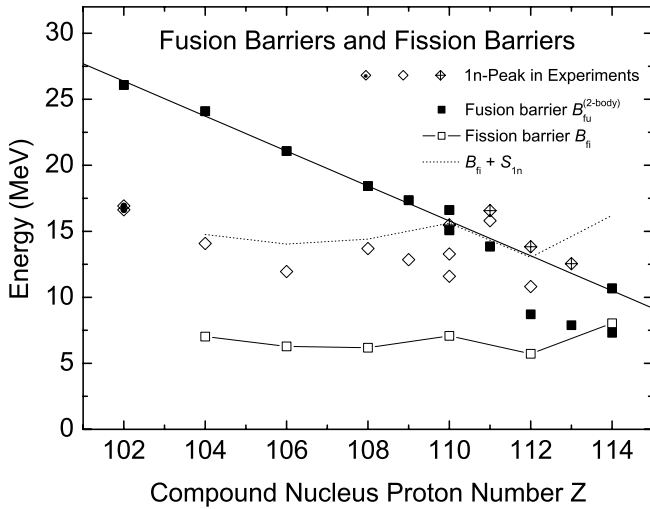


FIG. 10. Fusion-barrier height $B_{fu}^{(two-body)}$ compared to the compound-system fission-barrier height [29]. Both barrier heights are given relative to the compound-system ground-state energy. We also show the energy of the peak of the $1n$ cross section and the sum $B_{fi} + S_{1n}$ of the fission-barrier height and the $1n$ separation energy. Although we show only the fission-barrier heights for even-even nuclei for simplicity, $B_{fi} + S_{1n}$ for odd-odd nuclei follows the general trend of these even-even systems and is consistent with the experimental data. The peak energy of the $1n$ cross section for $^{270}110$ and $^{279}113$ is not available since there is only one data point for a fixed energy for each. In these cases, we identified the energy of the observed $1n$ channel as the peak energy.

channel is dominant at energies below $B_{fi} + S_{1n}$. Since the fusion cross section rapidly decreases below $B_{fu}^{(two-body)}$ and the energy corresponding to maximum survival probability is related to $B_{fi} + S_{1n}$, an analysis of the relation between $B_{fu}^{(two-body)}$, the sum $B_{fi} + S_{1n}$, and the most favorable collision energy is essential. The analysis may be most transparent if we give all energies relative to the ground state of the compound system.

We show these three quantities in Fig. 10. The solid squares denote $B_{fu}^{(two-body)}$. The open diamonds denote the experimentally determined energy of the maximum in the $1n$ cross section. The open diamonds and the open diamonds with superimposed dots and crosses denote the data from Dubna, GSI, and RIKEN, respectively. For these heavy compound systems, the highest saddle point on the fission barrier occurs just beyond the ground state. Its height relative to the ground state has been calculated versus three deformation coordinates, ϵ_2 , ϵ_4 , and γ . The calculation explores the full three-dimensional space and determines the saddle-point location in this space by a water-immersion technique. The corresponding fission-barrier heights are denoted by open squares connected by a thin solid line. $B_{fi} + S_{1n}$ is represented by a dotted line. The reaction Q value and the $1n$ separation energy are taken from [17]. Figure 10 clearly shows that our calculated fusion-barrier heights $B_{fu}^{(two-body)}$ decrease linearly as the value of the compound-nucleus proton-number Z increases. The

fusion-barrier heights $B_{fu}^{(two-body)}$ are lower than $B_{fi} + S_{1n}$ in the systems heavier than $Z = 110$. Thus, we expect for the heavy systems the optimum collision energy in the $1n$ channel will be determined by the sum of the saddle-point height B_{fi} just beyond the ground state and S_{1n} . It appears that the experimental data of RIKEN denoted by open diamonds with superimposed crosses are in very good agreement with $B_{fi} + S_{1n}$. Since for $Z \geq 110$, the calculated barrier heights $B_{fu}^{(two-body)}$ become comparable to $B_{fi} + S_{1n}$, our calculated results are consistent with the observed energy at the maximum of the $1n$ -channel cross section.

Since our barrier heights $B_{fu}^{(two-body)}$ are considerably higher than $B_{fi} + S_{1n}$ for ^{48}Ca , ^{50}Ti , and ^{54}Cr projectiles (Fig. 10), one would expect that the $1n$ channel is strongly suppressed for these three systems. In fact, because the $1n$ -channel excitation function is asymmetric in shape for the systems ^{48}Ca and ^{50}Ti in Fig. 9, it seems that an effect of the two-body channel is seen. However, to explain the very low energy of the $1n$ peaks, a subbarrier enhancement below $B_{fu}^{(two-body)}$ or a decrease of $B_{fu}^{(two-body)}$ over and above what we calculate from deformation effects is needed. In heavy-ion reactions with ^{208}Pb targets, it is well known that subbarrier enhancement of the fusion cross section occurs. In coupled-channel calculations, the mechanism is that the low-lying 3^- and 5^- states of the ^{208}Pb target [32] affect the barrier distribution. The effect lowers the barrier by several MeV. If we assume that our calculated $B_{fu}^{(two-body)}$ is the average energy of the barrier distribution, the most favorable energy for the $1n$ reaction would be lowered by approximately this amount. However, even if we take into account this coupled-channel effect, it is very difficult to explain the very low energy of the peak of the $1n$ cross section from our current results. To explain the experimental results, we would need to further decrease our calculated $B_{fu}^{(two-body)}$ by 3–5 MeV from their present values. If we further decrease all $B_{fu}^{(two-body)}$ by 3–5 MeV, in all heavy systems, then the peak energy of $1n$ channel is higher than $B_{fu}^{(two-body)}$ for all the studied systems. Then the evaporation-residue cross section would be determined by the sum $B_{fi} + S_{1n}$, which is actually consistent with the observed energies of the peaks of the $1n$ evaporation-residue cross sections.

One possible mechanism for the decreasing $B_{fu}^{(two-body)}$ is a change in the nuclear radius r_0 or the diffuseness a parameters in the two-body channel because of some quantum effect not taken into account in the macroscopic part of the FRLDM used to calculate the interaction energy. The surface energy and the corresponding nuclear-interaction energy in massive systems are very sensitive to these parameters. For example, if we change the radius parameter r_0 from 1.16 to 1.2 fm, the spherical barrier for ^{48}Ca incident on ^{208}Pb decreases by 5.9 MeV.

We do not have a sufficiently tested microscopic model to institute such changes of radius and diffuseness parameters on a case-by-case basis. Alternatively, one could consider a global change of the radius and diffuseness parameters in the macroscopic FRLDM. However, since these parameters are optimized globally, in particular to nuclear masses and fission barriers within the framework of the FRLDM, one would

need to perform global studies involving the systematics of nuclear masses and other quantities before a change of these parameters could be instituted with confidence.

VI. SUMMARY

We have pointed out that “standard” models of the barrier in heavy-ion reactions that assume that the target and projectile remain spherical during the collision and in which the barrier can be described as a sum of a simple Coulomb interaction and a short-range nuclear interaction are too simplistic to give results that are sufficiently accurate to provide insight into the physics of cold-fusion reactions leading to the formation of elements at the end of the periodic system.

To obtain a more realistic model, we have argued that it is necessary also to consider deformation of the target and projectile during the collision process. For systems of interest, we have calculated adiabatic, static heavy-ion macroscopic-microscopic “collision” potential-energy surfaces versus separation and target and projectile deformations. In this model the potential energy is calculated as a sum of the Coulomb and short-range nuclear interaction energies between spheroidal targets and projectiles, oriented tip-to-tip. The potential-energy model also contains terms that account for the deformation dependence of the macroscopic-microscopic self-energies of the deformed targets and projectiles relative to their self-energies at infinite separation. In cold-fusion reactions, the target remains spherical because of the strong stabilizing effect of doubly or near doubly magic proton and neutron numbers in the Pb or Bi target. The effect of deformations in the projectile lowers the fusion barrier in the two-body channel $B_{\text{fu}}^{(\text{two-body})}$

by about 3 MeV in the cold-fusion reaction leading to ^{256}No and by up to almost 15 MeV in the reaction leading to $^{277}\text{112}$, relative to the barrier in the macroscopic spherical model. The special configuration of a strongly deformed projectile and near spherical target is shown to resemble well the “fusion-valley” configuration in the potential-energy surface of the one-body composite system. The strongly overlapping configurations for two-body and one-body systems at near touching is supposed to be a typical feature of these reaction systems, which would favor a cold-fusion reaction.

For cold-fusion reactions with projectiles near ^{48}Ca , our calculated barrier heights $B_{\text{fu}}^{(\text{two-body})}$ are still higher than what is experimentally indicated by 5–10 MeV. We feel this is due to additional microscopic or dynamical effects beyond the deformation and shell effects considered here. The nuclear radius and diffuseness might not follow the simple macroscopic prescriptions we use here. Unfortunately, microscopic self-consistent calculations with different forces [33] obtain very different results for the radius and diffuseness parameters for different, equally plausible microscopic forces, so little guidance can currently be obtained from these studies. However, it is our hope that because we have here introduced an improved fusion-barrier model, the nature of the remaining sources of deviation may become more apparent.

ACKNOWLEDGMENTS

We are grateful to Dr. Y. Nagame for fruitful discussions and to Dr. S. Hofmann for providing us with experimental data.

-
- [1] S. Hofmann and G. Münzenberg, *Rev. Mod. Phys.* **72**, 733 (2000).
 - [2] Yu. Ts. Oganessian *et al.*, *Phys. Rev. C* **69**, 021601(R) (2004).
 - [3] Yu. Ts. Oganessian *et al.*, *Phys. Rev. C* **69**, 054607 (2004).
 - [4] K. Morita *et al.*, *J. Phys. Soc. Jpn.* **73**, 2593 (2004).
 - [5] W. J. Świątecki, K. Siwek-Wilczyńska, and J. Wilczyński, *Phys. Rev. C* **71**, 014602 (2005).
 - [6] P. Möller and A. Iwamoto, *Nucl. Phys.* **A575**, 381 (1994).
 - [7] H. J. Krappe, J. R. Nix, and A. J. Sierk, *Phys. Rev. C* **20**, 992 (1979).
 - [8] R. Bass, *Nuclear Reactions with Heavy Ions* (Springer-Verlag, Berlin, 1980).
 - [9] V. Yu. Denisov and W. Nörenberg, *Eur. Phys. J. A* **15**, 375 (2002).
 - [10] P. Möller and A. J. Sierk, *Nature* **422**, 485 (2003).
 - [11] A. Iwamoto, T. Ichikawa, P. Möller, and A. J. Sierk, *Nucl. Phys.* **A738**, 499 (2004).
 - [12] A. Iwamoto, P. Möller, J. R. Nix, and H. Sagawa, *Nucl. Phys.* **A596**, 329 (1996).
 - [13] S. G. Nilsson, *K. Dan. Vidensk. Selsk. Mat. Fys. Medd.* **29**, 16 (1955).
 - [14] P. Möller and J. R. Nix, *Nucl. Phys.* **A361**, 117 (1981).
 - [15] V. M. Strutinsky, *Nucl. Phys.* **A95**, 420 (1967).
 - [16] V. M. Strutinsky, *Nucl. Phys.* **A122**, 1 (1968).
 - [17] P. Möller, J. R. Nix, W. D. Myers, and W. J. Swiatecki, *At. Data Nucl. Data Tables* **59**, 185 (1995).
 - [18] P. Möller, A. J. Sierk, and A. Iwamoto, *Phys. Rev. Lett.* **92**, 072501 (2004).
 - [19] P. Möller and J. R. Nix, *Phys. Rev. Lett.* **37**, 1461 (1976).
 - [20] A. Sobiczewski, Z. Szymański, S. Wycech, S. G. Nilsson, J. R. Nix, C. F. Tsang, C. Gustafson, P. Möller, and B. Nilsson, *Nucl. Phys.* **A131**, 67 (1969).
 - [21] P. Möller, D. G. Madland, A. J. Sierk, and A. Iwamoto, *Nature* **405**, 785 (2001).
 - [22] J. R. Nix and A. J. Sierk, *Phys. Scr. A* **10**, 94 (1974).
 - [23] P. Möller and J. R. Nix, *Nucl. Phys.* **A272**, 502 (1976).
 - [24] Yu. Ts. Oganessian *et al.*, *Phys. Rev. C* **64**, 054606 (2001).
 - [25] A. V. Yeremin *et al.*, *JINR Rapid Commun. No. 6[92]-98*, 1998 (unpublished), p. 21.
 - [26] A. V. Belozerov *et al.*, *Eur. Phys. J. A* **16**, 447 (2003).
 - [27] H. W. Gäggeler *et al.*, *Nucl. Phys.* **A502**, 561c (1989).
 - [28] S. Hofmann (private communications).
 - [29] P. Möller, A. J. Sierk, T. Ichikawa, and A. Iwamoto, in *TOURS 2003, Tours Symposium on Nuclear Physics V, Tours, France*, AIP Conf. Proc. No. 704, (AIP, New York, 2004), p. 49.
 - [30] K. Morita *et al.*, *J. Phys. Soc. Jpn.* **73**, 1738 (2004).
 - [31] K. Morita *et al.*, *Eur. Phys. J. A* **21**, 257 (2004).
 - [32] C. R. Morton, A. C. Berriman, M. Dasgupta, D. J. Hinde, J. O. Newton, K. Hagino, and I. J. Thompson, *Phys. Rev. C* **60**, 044608 (1999).
 - [33] S. Yoshida and H. Sagawa, *Phys. Rev. C* **69**, 024318 (2004).